JOURNAL OF GEOPHYSICAL RESEARCH, VOL. 112, B06418, doi:10.1029/2006JB004302, 2007

Active salt tectonics in the Needles District, Canyonlands (Utah) as detected by interferometric synthetic aperture radar and point target analysis: 1992–2002

M. Furuya,[1,2] K. Mueller,[3] and J. Wahr[1]

Received 19 January 2006; revised 28 December 2006; accepted 22 February 2007; published 26 June 2007.

[1] The Needles District in Canyonlands National Park, Utah, is known for its well-exposed array of extensional faults, which are thought to be produced by gravity-driven extension and downward flexure of a thin sandstone plate into the Colorado River canyon in response to dissolution and flow of underlying evaporites (halite and gypsum). Owing to a lack of precise geodetic data, however, it remains uncertain if and to what extent those extensional faults are currently deforming. In this study we use synthetic aperture radar (SAR) data to search for ongoing, decadal ground displacements, by applying both a stacking interferometric SAR (InSAR) analysis and Interferometric Point Target Analysis (IPTA). Our results show that most of the Needles District is indeed undergoing deformation now at a maximum rate of 2–3 mm/year away from the satellite, looking roughly westward with an incidence angle of about 20°. Also, we identify a localized region along the riverbank that is uplifting at a rate of 2–3 mm/year. We estimate the measurement precision to be better than 0.8 mm/year, except along the riverbank where the errors are probably higher than this, by analyzing residual signals and carrying out a signal recovery experiment using synthetic two dimensional correlated noise. The deforming region is almost totally bounded by the Colorado River canyon to the west and north, a rapidly subsiding, east-west trending graben to the south, and a relatively sharp to very diffuse deformation gradient to the east. We observe deformation patterns that were previously undetected. These include an area in the southwestern part of the deforming region that is deforming at higher rates than anywhere else in the Needles but that has little surface extensional faulting. Rates of deformation are lower but still clearly significant further north, in a region of spectacularly exposed fault blocks that have been previously studied in considerable detail.

Citation: Furuya, M., K. Mueller, and J. Wahr (2007), Active salt tectonics in the Needles District, Canyonlands (Utah) as detected by interferometric synthetic aperture radar and point target analysis: 1992–2002, *J. Geophys. Res.*, *112*, B06418, doi:10.1029/2006JB004302.

1. Introduction

[2] Canyonlands National Park, located in southeastern Utah, is known for its spectacularly exposed landscapes of rocky surfaces and canyons, formed through sedimentation, erosion, and faulting over the past 300 million years (Figure 1). One of Canyonlands' more interesting regions is the Needles District, located southeast of the confluence of the Colorado and Green Rivers. The Needles contain strata that consist of a brittlely deforming sequence of Permian sandstone, overlying a mobile layer of evaporites (the Paradox Formation) that originated mostly as salt deposited during evaporation in restricted marine settings. Within the Needles is the Grabens region (Figure 1), which extends along the east side of the Colorado River 25 km downstream from its confluence with the Green River. This region includes elongate, parallel depressed blocks (grabens) bounded by normal faults that are separated by intervening higher blocks (horsts). These faults are thought to have been caused by the westward expulsion of underlying evaporites into the Colorado River canyon, and the subsequent downward flexure and extension of the overlying sandstone, and are interpreted to be currently active [e.g., *McGill and Stromquist*, 1979; *Trudgill and Cartwright*, 1994; *Schultz and Moore*, 1996; *Schultz-Ela and Walsh*, 2002; *Walsh and Schultz-Ela*, 2003]. The normal fault blocks in the Needles District offer opportunities to study the growth, interactions and linkages, of normal faults [e.g., *Trudgill and Cartwright*,

[1]CIRES and Department of Physics, University of Colorado, Boulder, Colorado, USA.
[2]Now at Earthquake Research Institute, University of Tokyo, Tokyo, Japan.
[3]Department of Geological Sciences, University of Colorado, Boulder, Colorado, USA.

0148-0227/07/2006JB004302$09.00

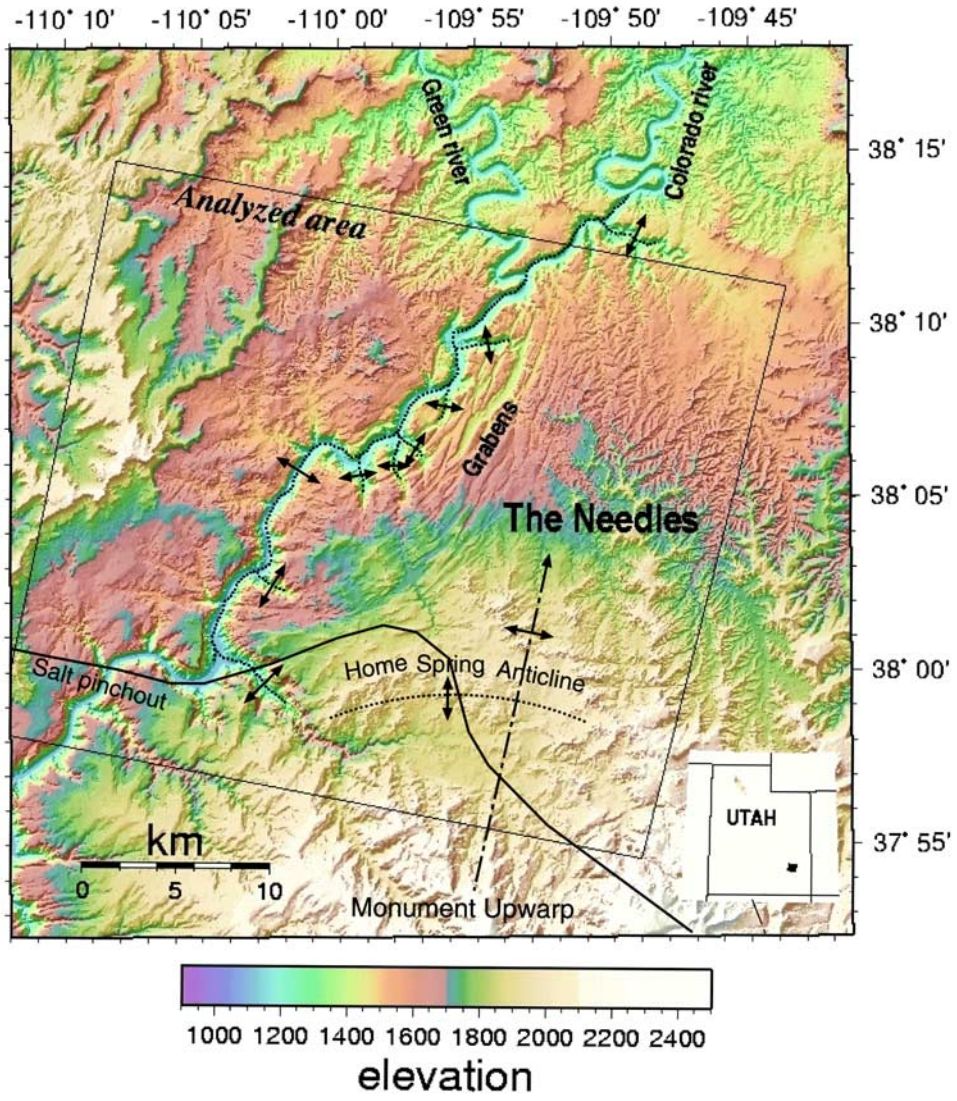

Figure 1. Topography, major geological structures, and location of the Needles District in Canyonlands National Park. The square area is used for the SAR data analysis. The inset shows the square's location relative to the Utah state boundary. Black dotted line denotes axis of the Meander Anticline along the Colorado River and smaller anticlines that correspond to side canyons to to the west. The Home Spring Anticline and the crest of the Monument Upwarp are also shown (latter as dash-dotted line). Folds are mostly redrawn from *Huntoon* [1982] and *Huntoon et al.* [1982]. Thick solid line indicates the location of salt pinchout toward the south [*Condon*, 1997].

1994; *Cartwright et al.*, 1995; *Schultz and Moore*, 1996; *Crider and Pollard*, 1998; *Moore and Schultz*, 1999; *Trudgill*, 2002; *Commins et al.*, 2005].

[3] There have been several numerical studies aimed at understanding the origin of the structural processes that are occurring in this region and the stresses that drive them [*Schultz-Ela and Walsh*, 2002; *Walsh and Schultz-Ela*, 2003]. Those studies assess long-term strain patterns using observations of surface faulting and folding, their relationship to Paleozoic strata of varied rheology, and numerical models of gravity-driven salt flow.

[4] The deployment of new, space-based, geodetic and remote sensing observing techniques offer additional opportunities for directly measuring rates of deformation and for relating maps of surface velocity to mapped faults, folds and salt diapirs. Over the last 2 decades, for example, GPS (Global Positioning System) measurements have been used to infer surface displacement rates in numerous regions of the world. Because of logistic problems (e.g., electricity, communication, and transportation), permanent GPS receivers have yet to be installed in the remote Needles District. Campaign-style GPS observations are thus an important means of assessing horizontal displacements in this region and are described by *Marsic et al.* [2003] and *Marsic* [2003].

[5] Interferometric Synthetic Aperture Radar (InSAR) observations provide a distinct advantage over campaign GPS measurements and provide almost complete spatial coverage at high resolution in a semiarid, sparsely vegetated region like the Needles District. InSAR is a satellite-based

remote sensing technique, capable of detecting millimeter-to-centimeter ground displacements through differential phase measurements of temporally separated SAR signals [e.g., *Massonnet and Feigl*, 1998; *Bürgmann et al.* 2000; *Hanssen*, 2001]. Standard InSAR processing methods use phase differences between pairs of satellite images (scenes), chosen such that the satellite positions for the two scenes are nearly coincident and the time difference is large. Recently, *Ferretti et al.* [2000, 2001] proposed a novel Permanent Scatterer technique, which makes use of stable point-target reflectors present in each scene. Once such scatterers are found with sufficient density, this technique allows the user to exploit the entire set of available scenes and to examine the temporal evolution of the displacement field [see also *Colesanti et al.*, 2003; *Werner et al.*, 2003; *Musson et al.*, 2004; *Hilley et al.*, 2004; *Hooper et al.*, 2004].

[6] The goal of this paper is to apply InSAR analysis, using both standard processing techniques and the method of Interferometric Point Target Analysis (IPTA) developed by *Werner et al.* [2003] (conceptually similar to the Permanent Scatterer technique), to make direct observations of ongoing ground displacements in the Canyonlands region. We also present a signal recovery experiment using synthetically generated spatially correlated noise so that we can quantify measurement errors. We compare the overall characteristics of the regional displacement field with those predicted from numerical studies and field observations.

[7] This is not the first InSAR study of the Needles District. *Marsic et al.* [2003] and *Marsic* [2003] applied standard InSAR techniques to determine the on-going displacement field. Our analysis extends and modifies these earlier studies in several ways. These include our use of the IPTA technique to complement the standard processing method, our employment of a stacking approach and an error analysis that are new and more robust, and our inclusion of far more scenes acquired over a longer time period. We are able to map time series movement of individual points on the ground surface at ~10 m resolution.

[8] Analysis of InSAR data is limited by the number of scenes used and the time period over which these data are acquired [*Emardson et al.*, 2003]. Previous analysis of InSAR data in Canyonlands was based on stacked interferograms acquired over a period of 5 years [*Marsic*, 2003], which is more than adequate for a region deforming at rates comparable to this area. Our error analysis suggests, however, that three or four independent interferograms are not sufficient to generate reliable results for signal amplitudes on the order of a few mm/year. Another limitation is the use of the same scene in an interferogram stack, such as the 22 June 1993 data used in the analysis of *Marsic* [2003]. *Marsic* [2003] considers this issue and uses local point-wise weather observations to argue that atmospheric errors in that scene were minimal. However, atmospheric signals can easily generate 10 mm of zenith delay even in the absence of rainfall [e.g., *Hanssen* 2001], which would be large enough to mask a small deformation signal on the order of a few mm/year. Moreover, our IPTA atmospheric solutions described below, indicate that the 22 June 1993 data does contain large atmospheric signals from around the grabens to the northeast (see supplementary Figure S1[1]).

2. Geological Background

[9] The array of extensional faults exposed in the Needles District covers an area of about 200 km^2 on the eastern side of the Colorado River, south of its confluence with the Green River (Figure 1) [e.g., *McGill and Stromquist*, 1979; *Huntoon*, 1982; *Trudgill and Cartwright*, 1994; *Cartwright et al.*, 1995; *Schultz and Moore*, 1996]. Most full grabens are between 100 and 500 m in width [*Huntoon et al.*, 1982] and intervening horsts are somewhat broader and about 200–700 m wide [*Huntoon et al.*, 1982]. Normal faults comprise an array that extends 6–10 km east of the river. These faults generally strike NNE, parallel to the trace of the Colorado River. Normal faults change their orientation in the southern part of the array, where they strike east-west adjacent to the Colorado River Canyon.

[10] Strata exposed in the Needles District includes ~450 m thick sequence of Pennsylvanian to early Permian sandstones and limestones that overlay evaporite deposits of the Paradox Formation. Extension of Pennsylvanian–Permian strata in the Canyonlands region is believed to have been initiated within the last 0.5 Ma, by incision of the Colorado River into the Paradox Formation [see, e.g., *McGill and Stromquist*, 1979; *Schultz-Ela and Walsh*, 2002; *Walsh and Schultz-Ela*, 2003]. The region east of the river dips northwest at ~2° on the northwest flank of the north-trending Monument Upwarp (Figure 1), a fold created during the early Tertiary Laramide orogeny. Downcutting of the Colorado River thus removed sedimentary strata that buttressed the west-dipping limb of the Monument Upwarp. That region was then free to spread westward toward the river, gravitationally driven by the 2° slope of the Paradox Formation and older strata. Expulsion and dissolution of halite along the eastern edge of the Colorado River then produced downward flexure of the brittle, overlying strata. In addition, salt diapirs formed adjacent to the eastern margin of the river canyon, in association with upward flexure of a fold termed the Meander Anticline that closely corresponds to the trace of the Colorado River (Figure 1) [*Huntoon*, 1982; *Huntoon et al.*, 1982; *Schultz-Ela and Walsh*, 2002]. Flexure of the brittle 450 m thick plate east of the river is believed to be followed by extension, where steeply dipping normal faults propagate downward from Earth's surface into the underlying salt layer [*Schultz-Ela and Walsh*, 2002]. The southern extent of the subsiding region east of the river corresponds with another E–W trending fold, the Home Spring Anticline (Figure 1) [*Huntoon et al.*, 1982].

[11] Using the InSAR technique described below, we identify surface velocity fields associated with many of the features summarized above. These include a pattern of overall increase in the line-of-sight (LOS) range due probably to subsidence of the region between the crest of the Monument Upwarp and the river, with large subsidence related to broad plate flexure southwest of the main fault array; little or no displacements east of the Monument

[1] Auxiliary materials are available in the HTML. doi:10.1029/2006JB004302.

Table 1. ERS1/2 Data

Date, yyyymmdd	Satellite	Orbit Number
19921124	E1	7114
19921229	E1	7615
19930413	E1	9118
19930518	E1	9619
19930622	E1	10120
19930831	E1	11122
19931109	E1	12124
19950406	E1	19482
19950511	E1	19983
19950824	E1	21486
19950825	E2	1813
19951102	E1	22488
19951103	E2	2815
19951208	E2	3316
19960530	E1	25494
19961018	E2	7825
19961122	E2	8326
19961227	E2	8827
19970516	E2	10831
19970829	E2	12334
19971003	E2	12835
19971107	E2	13336
19990312	E2	20350
19990521	E2	21352
19991008	E2	23356
19991112	E2	23857
19991217	E2	24358
20000121	E2	24859
20000505	E2	26362
20000609	E2	26863
20000714	E2	27364
20000818	E2	27865
20000922	E2	28366
20011012	E2	33877
20020405	E2	36382

Upwarp axis, which indeed should be unaffected by modern salt flow related to the downcutting of the Colorado River; upward displacements along the Colorado River that correspond in part to the mapped location of individual salt diapirs and the Meander Anticline [*Huntoon*, 1982]. Finally, our work defines an abrupt LOS-velocity gradient at the eastern edge of this array, in the region that is highly extended by NNE-trending normal faults, whereas this gradient becomes remarkably diffuse to the south, in the region where little surface extension is evident.

3. SAR Data Analysis

[12] We use C-band (wavelength 5.6 cm) SAR data from two European Remote Sensing satellites, ERS1/2, that include 35 scenes taken from frame 2835 of descending track 456 (see Table 1). To reduce our computational effort, as well as to avoid vegetated regions where low coherence is expected, we only use the portion of each scene shown within the square outline of Figure 1. The satellite track passes east of this region. Topographic fringes are reduced using a 1/3 arcsec (~10-m) grid digital elevation model (DEM) from the USGS National Elevation Dataset. We use orbital information provided by Delft Technical University [*Scharroo and Visser*, 1998] to reduce orbital fringes.

[13] An InSAR image provides estimates of displacements along the LOS. Because we use scenes from only one descending track, we are able to obtain displacement estimates along only one LOS direction. Adding data from an ascending track would give us displacements in a second direction, and so would help resolve the full three-dimensional (3-D) displacement fields over this area. However, there are too few ascending track data available to obtain a stacked result that is accurate enough to usefully combine with the descending stack. Even from the descending track data alone, however, we are able to recover significant results for both the signal amplitude and the locations of actively deforming regions.

[14] Errors in the DEM and orbit models cause errors in the InSAR displacement estimates. In addition, atmospheric propagation delays can cause measurable phases in interferograms, resulting in apparent displacements of up to a few centimeters or more [e.g., *Hanssen*, 2001]. Atmospheric delays are typically coherent at scales longer than several kilometers but tend to be temporally random and so can be reduced by combining results from many scenes. The effects of an orbit error appear as a spatial constant plus slope across the image. Since orbit errors should be uncorrelated between scenes, combining many scenes thus reduces them as well.

[15] We processed SAR data from the level-0 product, using a software package from Gamma Remote Sensing [*Wegmüller and Werner*, 1997; *Werner et al.*, 2003]. We use both a standard InSAR processing scheme [e.g., *Massonnet and Feigl*, 1998; *Bürgmann et al.*, 2000; *Hanssen*, 2001] and an IPTA technique. For our standard approach we select pairs of scenes with short perpendicular baselines and long temporal separation. The baseline is the distance between the satellite's locations for the first and second scenes; the perpendicular baseline is the baseline component perpendicular to the LOS from the spacecraft to the ground. The perpendicular baselines must be short to minimize the effects of DEM errors. Here we choose pairs with perpendicular baselines shorter than 50 m and with temporal separation greater than 700 days to accentuate the displacement signal (see Table 2). We choose pairs such that no scene is included in more than one pair and obtain 11 pairs of independent interferograms.

[16] Standard InSAR techniques are used to generate differential interferograms for each pair. These are spatially averaged over a ~50 m × 50 m window. The 11 interferograms are averaged together (stacked) to obtain a final estimate of the linear displacement rate at each location. Stacking reduces the effects of atmospheric refraction, orbit error slope, and nonlinear ground displacements (e.g., any

Table 2. Description of the 11 Independent Interferograms

Figure	Date 1	Date 2	Bperp,[a] m	Time, days
3a	24 Nov 1992	12 Nov 1999	−36.0	2544
3b	13 Apr 1993	2 Nov 1995	27.3	933
3c	18 May 1993	18 Aug 2000	−14.5	2649
3d	22 Jun 1993	21 Jan 2000	44.6	2404
3e	31 Aug 1993	21 May 1999	39.9	2089
3f	9 Nov 1993	8 Dec 1995	−25.3	759
3g	24 Aug 1995	12 Mar 1999	−6.1	1296
3h	18 Oct 1996	5 Apr 2002	−35.0	1995
3i	29 Aug 1997	17 Dec 1999	−47.3	840
3j	3 Oct 1997	5 May 2000	−40.0	945
3k	7 Nov 1997	8 Oct 1999	−11.6	700

[a]Bperp stands for perpendicular baseline.

seasonal or irregular motion caused by processes such as swelling of soils, episodic tectonic activity, etc.). By subtracting the stacked displacement rate from the 11 sets of displacement rates, we find the RMS scatter of the residuals. It should be noted that the scatter is not necessarily all noise but could also be partly due to episodic tectonic motion; we will argue this point later on. We describe in detail the processing steps for our IPTA analysis in Appendix A.

4. Results: Broad Perspective

4.1. Linear Deformation Rate and Error Estimate

[17] Secular displacements were first estimated using the standard stacking technique, using the 11 original interferogram pairs in Figure 2. Figure 3a shows the mean yearly rate of LOS change from the standard stacking described in section 3; its oblique view from the north-northwest is shown in Figure 4. The signal in the grabens, and the even larger signal southwest of the grabens, stand out clearly, with a maximum displacement amplitude on the order of $\sim$3 mm/year. The deforming region is restricted to east of the river. Moreover, Figure 3 shows a narrow zone of LOS shortening of about 2–3 mm/year, lying within the river canyon just west of the grabens; see also Figure 4. While there is a caveat on this shortening signal, as discussed below, that signal probably represents surface uplift associated with diapiric motion of salt, since the shortening regions can be correlated with the mapped locations of individual salt diapirs and the eastern limb of the Meander Anticline along the Colorado River [*Huntoon et al.*, 1982; *Jackson et al.*, 1994; *Baars*, 2003]. This is the first geodetic detection of an uplift signal in this region and is not reported in previous studies. Although this localized shortening can only be seen in isolated areas, the steep topography near the river causes radar shadow and layover problems that may obscure the detection of a continuous zone of LOS shortening.

[18] The displacement amplitude is 2$\sim$3 mm/year, which is smaller than most previously reported InSAR signals. We present below three lines of evidence that allow us to assess the reliability of the inferred deformation signal throughout the Needles, and that provide estimates of measurement errors.

[19] The first line of evidence comes from a scrutiny of the interferograms. The original interferograms shown in the first and third columns of Figure 2 display no spatially persistent signals that obviously suggest the existence of secular ground deformation. Also, the amplitude itself varies notably from pair to pair. Although this is partly due to differences in the time span of each interferogram, these amplitude differences between pairs suggest that the deformation signal is masked by much larger atmospheric propagation delays and illustrate the potential error involved in relying on a single interferogram to estimate trends. However, there are clear signal discontinuities across the Colorado River in many of the images shown in the first and third columns of Figure 2. Since it is unlikely that atmospheric effects would change discontinuously across the river, we suspect that those discontinuities reflect real motion of the surface. This suspicion is reinforced by looking at ''residual'' interferograms in the second and fourth columns of Figure 2, generated by subtracting the stacked linear deformation (Figure 3a), scaled to each time separation, from each original interferogram. Although these residual interferograms are still noisy in places, the discontinuities across the Colorado River have now disappeared, and the color patterns have become more continuous. The implication is that each of the original interferograms is consistent with the discontinuity present in Figure 3a, and so that discontinuity is probably real. The residual interferograms are probably mostly caused by local atmospheric effects.

[20] Regarding the LOS shortening signal along the river, however, we suggest caution is required when interpreting the individual interferograms. Although we will discuss this issue in more detail in section 4.2, large elevation changes can generate so-called ''topography-correlated atmospheric errors.'' On one hand, we can clearly recognize LOS shortening signals in long-temporal separation pairs such as Figures 2a, 2c, 2e, 2g, and 2h. On the other hand, Figure 2d does not reveal such signals despite its long temporal separation of 2404 days. Moreover, Figure 2j shows unexpectedly large LOS shortening amplitudes despite its relatively short temporal coverage. These complexities arise not only from the small amplitude of the LOS shortening but also from random atmospheric effects. This argues against relying on just a few interferograms and suggests that a more robust approach is necessary. Both our stacking and IPTA results show that the uplifting signals are significant.

[21] The second line of evidence for signal reliability is the LOS displacement rate shown in Figure 3b derived from the IPTA technique. Since the threshold requirements used in the IPTA approach reduce the density of recovered points, fewer points are shown in Figure 3b than in Figure 3a particularly along the riverbank; we discuss this point in the next section. We also note that there are some isolated spurious points with higher/lower deformation rates, where we do not find corresponding higher/lower rates in Figure 3a. Although these points have been preserved in the IPTA processing, we suggest that the isolated points represent noise. Nevertheless, it is apparent that both the pattern and the amplitude of the signal shown Figure 3b are in good agreement with those shown in Figure 3a. In the IPTA technique, we have used 13 additional independent scenes that were not used in the standard stacking technique, which reduce the uncertainty in the linear trend estimate.

[22] The third line of evidence for the reliability of the signal is from a signal recovery experiment. Shown in Figure 5a are power spectra of the residual interferograms in Figure 2, which we assume are mostly due to atmospheric effects. We assume those effects are distributed isotropically in orientation, and thus plot their one-dimensional spectra. The spectra show a power-law behavior, with an absolute value that fluctuates over one order of magnitude, depending on which pair of scenes was selected. This is consistent with the expected behavior of atmospheric signals, as discussed by *Hanssen* [2001]. We have generated 11 synthetic two-dimensional data sets that mimic the power-law behavior shown in Figure 5a. The power spectra of these synthetic data are shown in Figure 5b; a sample two-dimensional synthetic interferogram is shown in Figure 6. In order to evaluate the measurement precision of our present stacking analysis, we generate 11 synthetic interferograms, each consisting of

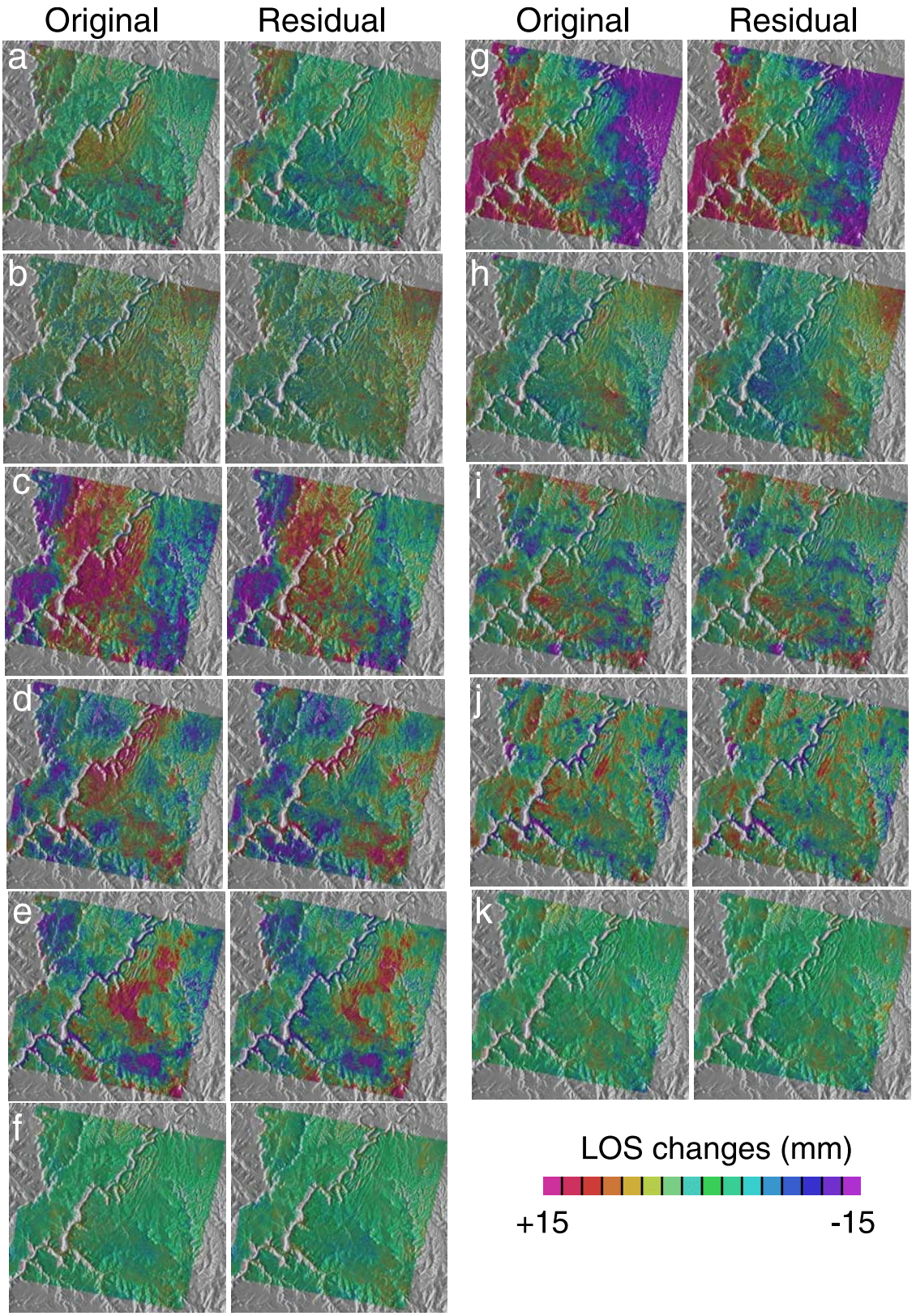

Figure 2. The 11 independent differential interferograms used in the standard stacking analysis. The left and right columns denoted as original and residual are before and after removal of a linear deformation trend, respectively. A positive line-of-sight (LOS) value implies motion away from the satellite. See Table 2 for the acquisition date of each pair.

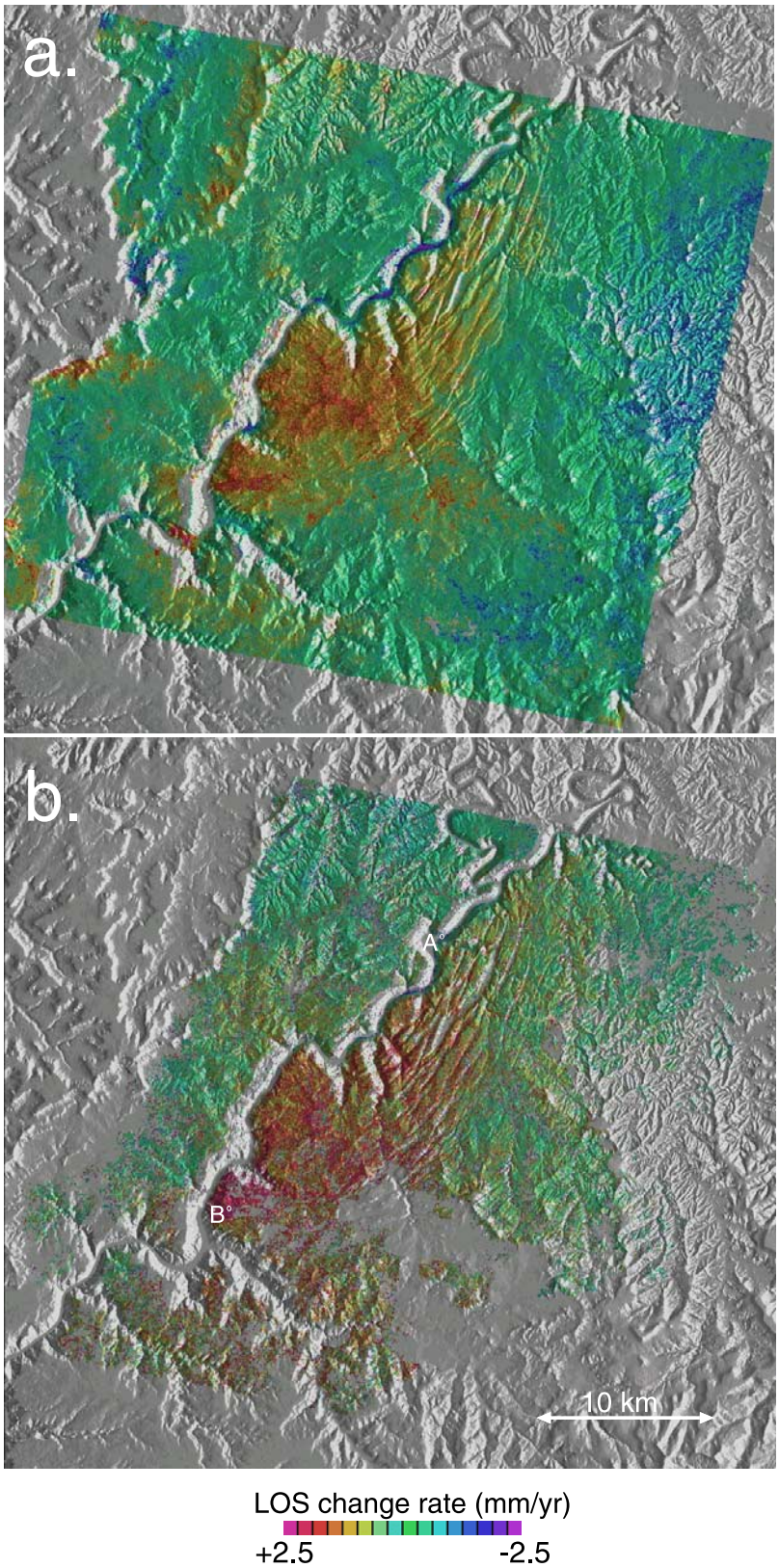

Figure 3. (a) The mean yearly displacement rates along the radar LOS (positive is away from the satellite), obtained by stacking the 11 interferograms in Figure 2. (b) Same data derived from the IPTA technique. The background gray image is a simulated backscatter intensity image. See Figure 8 for time series data at point A and B.

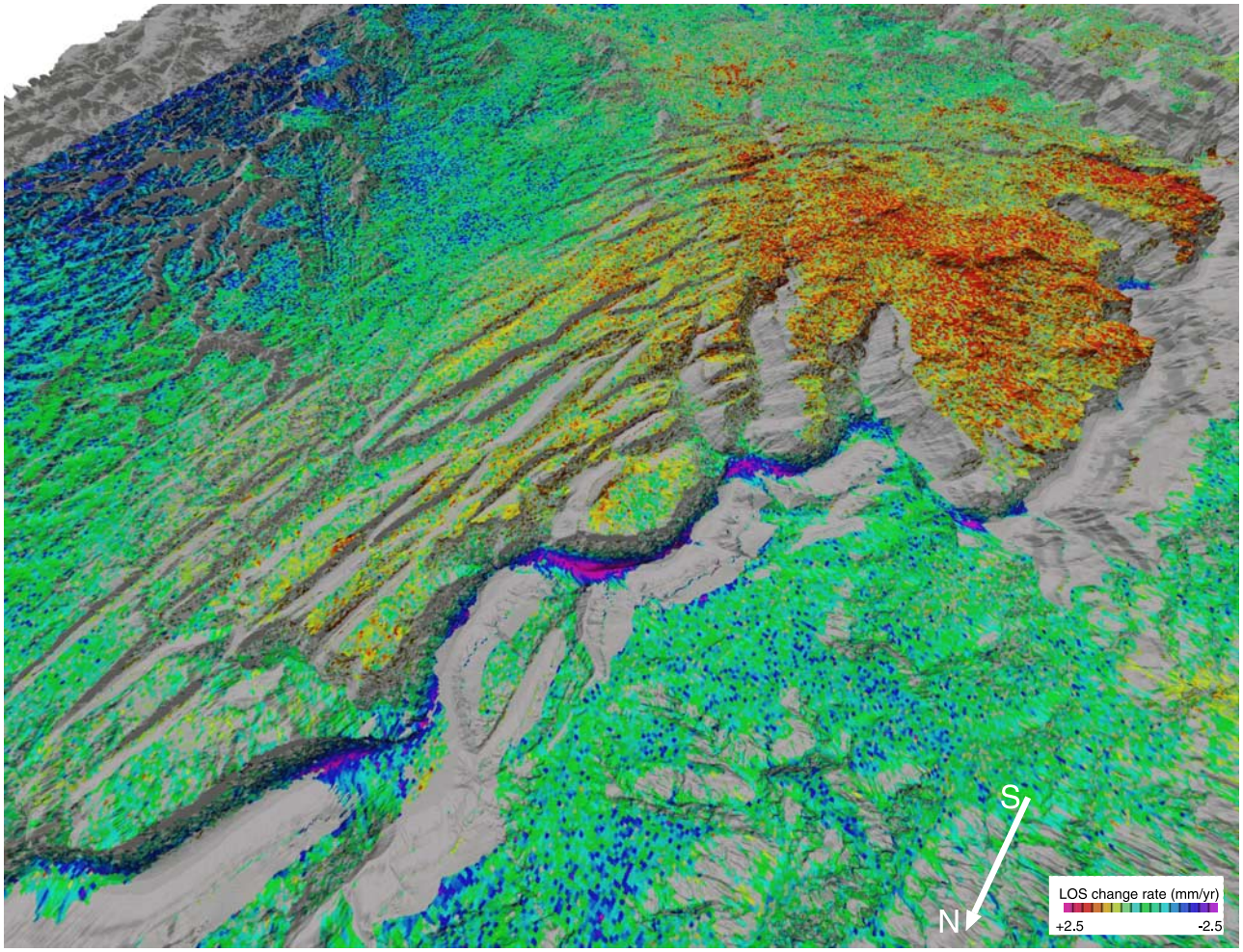

Figure 4. Oblique view of the mean yearly displacement rates draped on the topographic relief map; this is viewed from NNW. Portions of the region cannot be imaged because of lay-over and shadow problems inherent to a side-looking radar system. Displacements rates are the same as in Figure 3a.

synthetic noise of the form shown in Figure 6, added to the inferred linear deformation rate in Figure 3a multiplied by the average time span of the 11 pairs (4.3 years). Next, we stacked these synthetic data in the same way we stacked the real data to see if and to what extent we can recover the "hidden" deformation signal as masked by atmospheric effects. Figures 7a and 7b show the recovered linear deformation rate and the difference in absolute value between Figure 3a and Figure 7a, namely the measurement error. Both the original and the recovered linear trend are in good agreement. The difference shown in Figure 7b can be regarded as the estimation error for the linear deformation rate. Here 90% of all pixels have errors of less than 0.8 mm/year. Although not shown here, we conducted other experiments. They showed that as we reduced the number of pairs, and reduced the average time separation, it became increasingly difficult to recover the original linear deformation signal. As noted by *Emardson et al.* [2003], the fewer the number of interferograms and the shorter the temporal separation, the larger the deformation amplitude must be to robustly infer a linear deformation rate. Our present case of 11 pairs with an average of 4.3 years appears to be sufficient to derive the deformation signal with errors of ±0.8 mm/year up to a horizontal scale of ~30 km.

[23] Figures 3a and 3b both indicate that there is significant deformation throughout the western section of the Needles District, east of the Colorado River, including in both the array of normal faults to the north and the region of little obvious surface extension located to the south. The LOS displacement rates in the grabens range from 1.0 to 2.0 mm/year, away from the satellite. Larger deformation rates are observed further southwest, where there are no clear graben/horst structures, in the wedge-shaped region bounded on the north and west by the river. The LOS displacement rates in that area are 2.0–3.0 mm/year away from the satellite. Moreover, in the southern portion of this area there appears to be a sharp offset in the LOS changes with a signal greater than 2.0 mm/year signal that is coincident with a large, east-west trending graben that bounds the southernmost extensional fault in the region (Figure 1). The region of large displacement rates terminates abruptly across the north-dipping normal fault that bounds the graben. We note the east-west trending graben lies immediately north of the similarly oriented edge of the Permian basin, where evaporite facies pinch out (i.e., are not

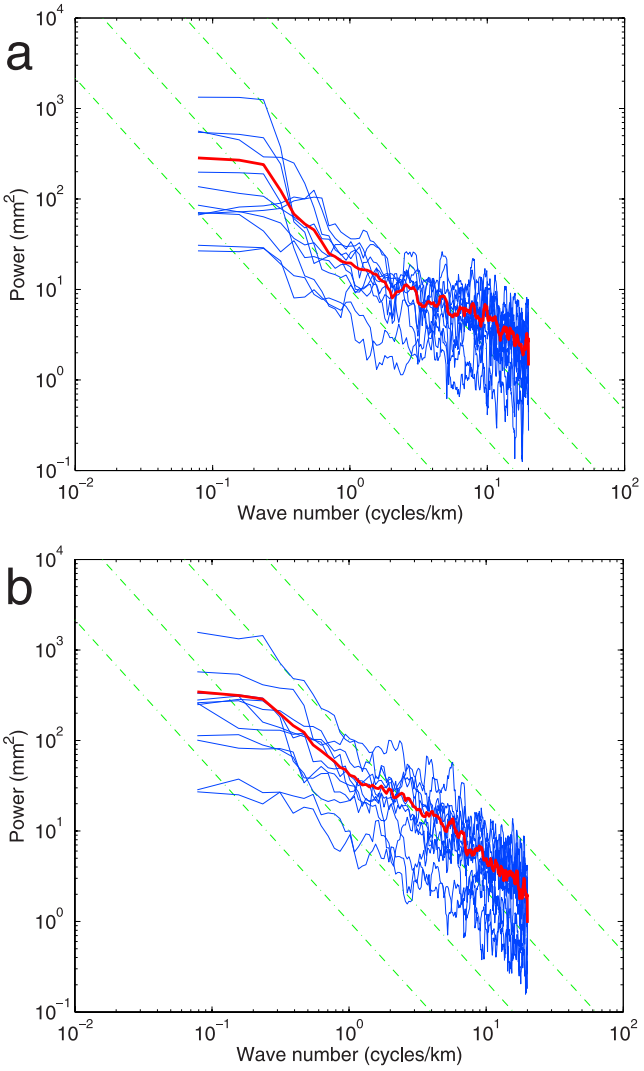

Figure 5. (a) Power spectra for the residual interferograms in the 2nd and 4th columns of Figure 2. (b) Same spectra for the 11 synthetic noise data sets; a sample two dimensional interferogram of this noise is shown in Figure 6. Red is the average of the 11 spectra. Dash-dotted lines are for noise spectra with a power-law frequency dependence of −5/3.

present to the south) along the north-dipping limb of the Home Spring Anticline (Figure 1).

4.2. Atmospheric Effects and Possible Nonlinear Deformation

[24] In contrast to the standard stacking approach, which acts on pairs of scenes, the IPTA technique allows us to infer phase values for each of the 35 scenes individually and so to develop a time series at each point. At the end of the third iteration of (A1) (i.e., after step 11 in Appendix A), we have estimated a linear velocity (v) at each reflector, and have obtained residual values (residual$_j$) for each scene. Figure 8 shows two representative time series data derived from the IPTA technique at points A and B in Figure 3b. Both time series show significant secular trends.

[25] The residual values include contributions from atmospheric refraction, orbit error slope, and nonlinear

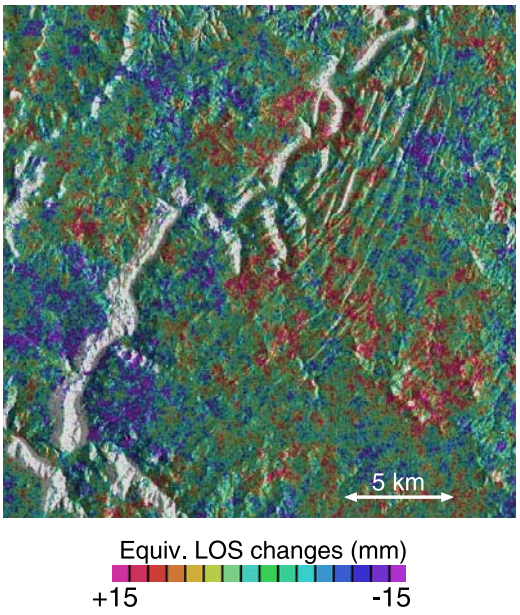

Figure 6. An example of two-dimensional correlated noise, which was synthetically generated and added to a deformation signal in the signal recovery experiment.

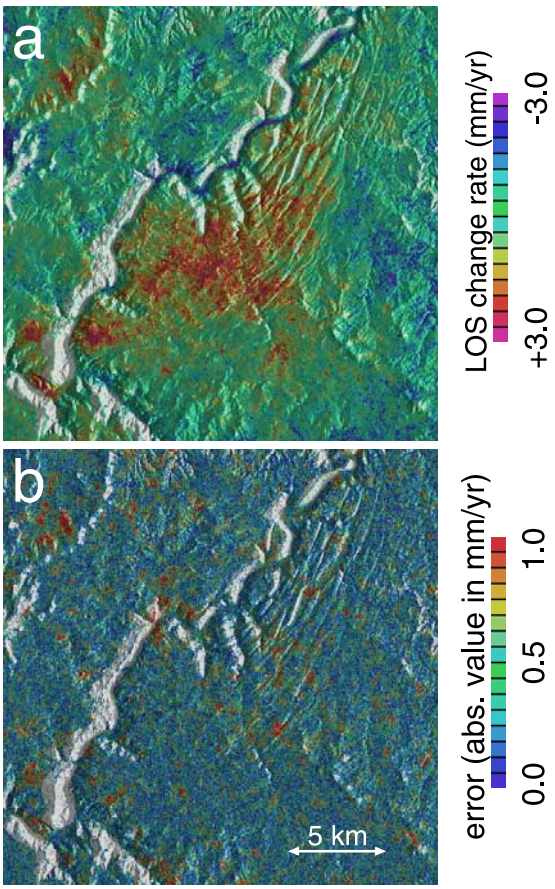

Figure 7. (a) The mean yearly displacement rates along the radar LOS, recovered from 11 synthetic interferograms. (b) The difference in absolute value between the recovered and the "true" rate in Figure 3a.

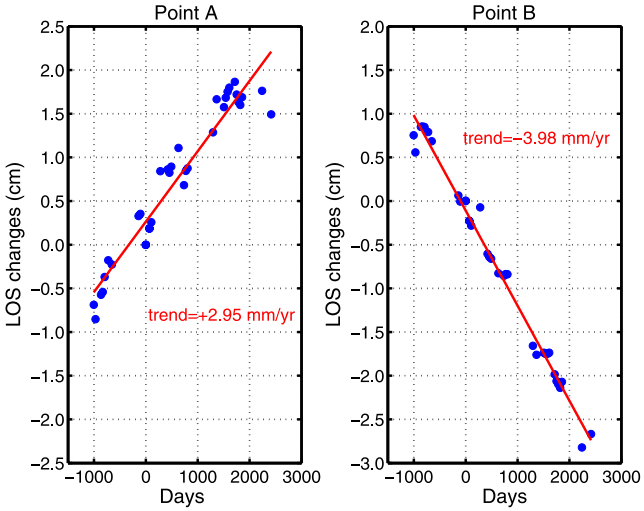

Figure 8. LOS change time series data at point A and B in Figure 3b derived from the IPTA analysis. The horizontal axis represents deviations in days with respect to August 25, 1995.

ground displacements. Figure 9 shows the root-mean-square (RMS) values of the residuals from the 35 scenes (Figure S1). We suspect that much of the variability shown in Figure 9 represents atmospheric refraction effects and orbit errors. Figure 9 shows that the RMS is lowest near the reference point, 38.1761°N, 109.9817°W, and tends to increase monotonically with distance from the reference point. Since the differential phase, ϕ^j_{diff}, is set to zero at the reference for each scene j, and since the residual is by definition a deviation from the phase model (see (A1)), it is quite reasonable that the RMS values near the reference point take minimum values. The RMS value at any other point then largely reflects the difference between the non-linear phase variability at that point and that at the reference point. Both atmospheric signals and orbit errors are spatially correlated over a few km or more [*Hanssen*, 2001; *Emardson et al.*, 2003; *Lohman and Simons*, 2005] and temporally random. Thus it would be expected that the RMS would tend to be small at locations near the reference point and larger at locations further away, consistent with Figure 9.

[26] One notable exception in Figure 9 is the narrow trace of large RMS values adjacent to the Colorado River that differ significantly from neighboring RMS values. At first glance, it is unlikely that atmospheric effects would be horizontally localized to this extent. However, the elevation difference between the bottom of the canyon and the surface of the grabens ranges from ~400 m in the north to over ~600 m in the southwest. As briefly mentioned in the previous section, it is empirically known that noisy fringes can be correlated with topography, presumably due to atmospheric effects [e.g., *Hanssen*, 2001; *Emardson et al.*, 2003; *Lohman and Simons*, 2005]. Although we cannot completely rule out the possibility of nonlinear deformation, it is more likely that the large RMS values are due to topography-correlated atmospheric effects. Nonetheless, the decreasing trend in the LOS change near the river is significant as clearly seen in Figure 8; the point A indeed shows larger temporal fluctuation around the mean trend in contrast to that in point B. While many of those large RMS points coincide with the points in Figure 3 that show a large decrease in the LOS near the river, it should be noted that not all the points with large RMS show a secular decrease in the LOS; some of the points in the side canyon show an LOS increase.

[27] Figure 10 is a standard deviation map derived from the standard stacking technique, which again includes not only nonlinear deformation but also atmospheric and orbit error effects. Although the derived standard deviation is 1.0–2.5 mm/year averaged over the entire figure, we observe large standard deviation values basically in two areas; other than these, the standard deviations are generally less than 1 mm/year, which is consistent with our estimated 0.8 mm/year. One area is in the eastern and western edges of the scene, and the other area is along the river. In the former large standard deviations can be interpreted as caused by orbit errors and atmospheric effects, because those tend to generate long-wavelength noise. The large standard deviation is again seen in a localized region along the river, in a location that closely matches the region of large RMS in Figure 9. Elevation changes can generate large topography-correlated errors as noted above, which would not be taken into account in our spatially isotropic synthetic two-dimensional noise. This could explain the difference between our estimated errors of 0.8 mm/year and the overall standard deviation of 1.0–2.5 mm/year. We see therefore that the signal amplitude along the river becomes comparable to the standard deviation in some places. However, in view of the systematic spatial trend inferred from the cross section profiles in Figure 12 discussed below, as well as the distinct secular trend at Point A in

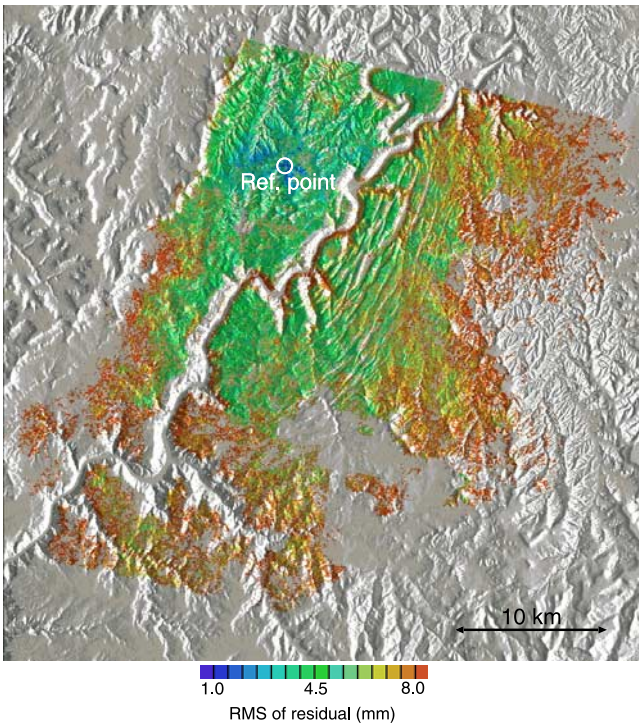

Figure 9. Root-mean-square (RMS) values of the 34 residual values in the IPTA analysis.

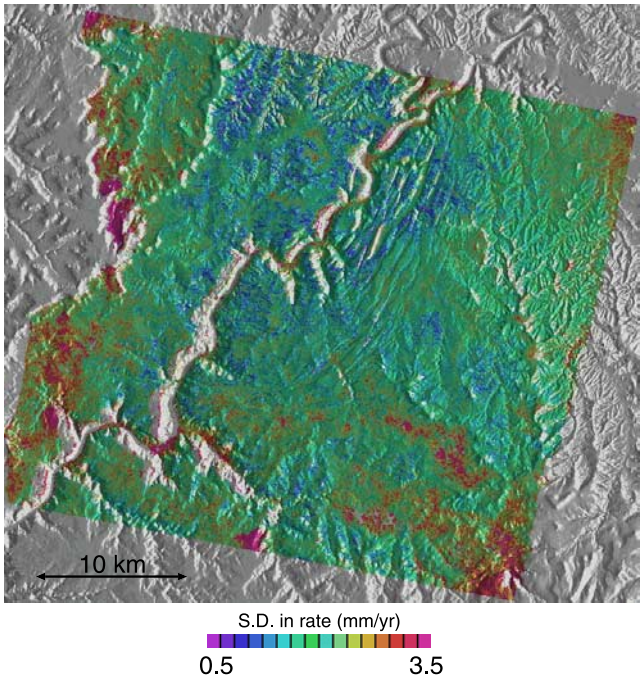

Figure 10. Standard deviation map of the inferred rate in Figure 3a.

Figure 8, it is likely that the signal along the river reflects actual uplift of the surface.

5. Discussion

[28] Since we have only been able to acquire data from the descending track and so have LOS estimates along only one look direction, it is not possible to determine the vertical and horizontal components separately. We note, though, that with the present descending track data the LOS displacement is ~0.9 × subsidence + 0.3 × westward displacement + 0.1 × southward displacement. Thus it is unlikely that north-south displacements contribute significantly to the results. A LOS displacement of +3 mm/year could imply subsidence of 3 mm/year, or westward motion of 9 mm/year, or some combination of those two components. According to the GPS results from *Marsic* [2003], however, no GPS sites showed horizontal velocity significantly larger than 5 mm/year, although the six GPS sites with one reference station were installed only in the eastern area of the Needles. The small amplitude of the GPS data does rule out the possibility that the increases in the LOS in the Needles are caused by horizontal displacements. Additional GPS data could provide a strong constraint for the interpretation of future InSAR data.

[29] In order to examine the velocity fields in Figures 3 and 4 and their correspondence to surface structures such as grabens, horsts, canyons, fault traces, and topography, we extract LOS velocity and elevation values along the seven selected profiles shown in Figure 11; results are shown for the standard stacking approach. Fault traces in Figure 11 are registered from those in the work of *Trudgill* [2002, Figure 1] to our InSAR image (Figure 3); the only exception is the fault trace passing through GG' in the southwest that we have drawn based on prior mapping by *Huntoon et al.*

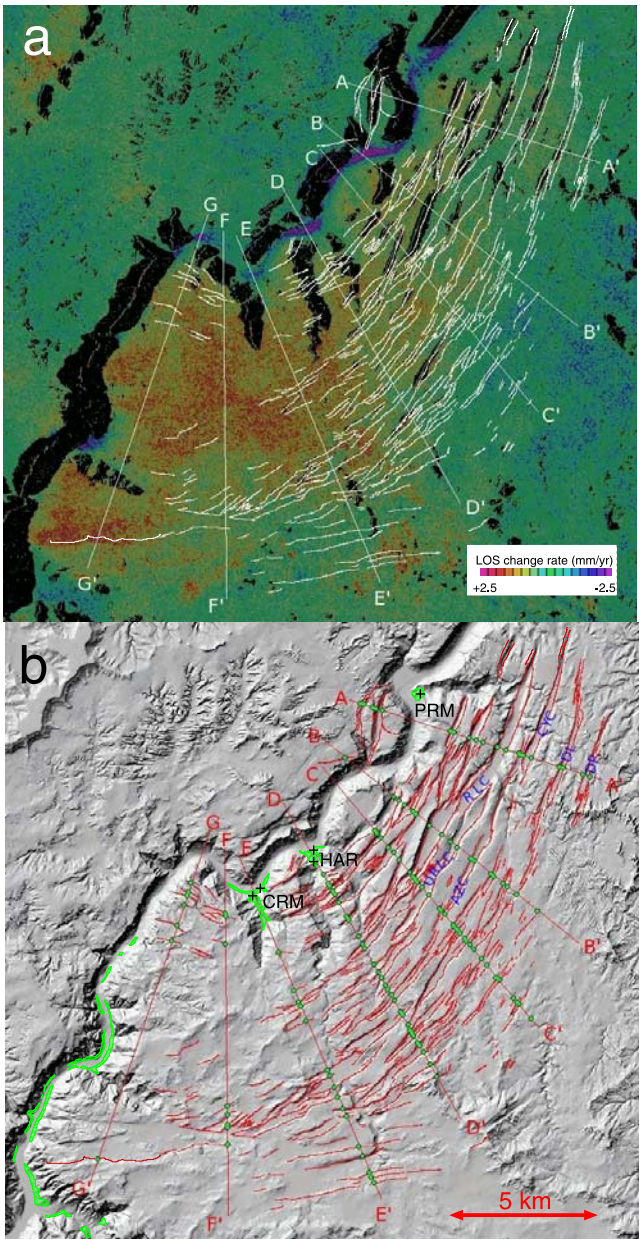

Figure 11. (a) Mean yearly displacement rates (positive is away from the satellite) with fault traces and surface tracks for the cross sections in Figures 12; fault traces are redrawn from *Trudgill* [2002] with one exception in the SW running through GG' profile (see texts). Displacement rate data are derived from the standard stacking approach. (b) Fault traces and surface tracks draped on a shaded relief map. Green dots represent cross-over points of surface tracks to the fault traces, and are the locations for the vertical lines in Figures 12. Canyon names in blue for annotated abbreviations are as follows. RLC: Red Lake Canyon, CYC: Cyclone Canyon, DL: Devil's Lake Canyon, DP: Devil's pocket Canyon, URLC: Upper Red Lake Canyon, AZC: Aztec Canyon. Light green areas are the salt exposures, and salt domes are indicated with positive signs. PRM: Prommel, HAR: Harrison, CRU: Crum. Geological structures are mostly redrawn from *Huntoon* [1982] and *Huntoon et al.* [1982].

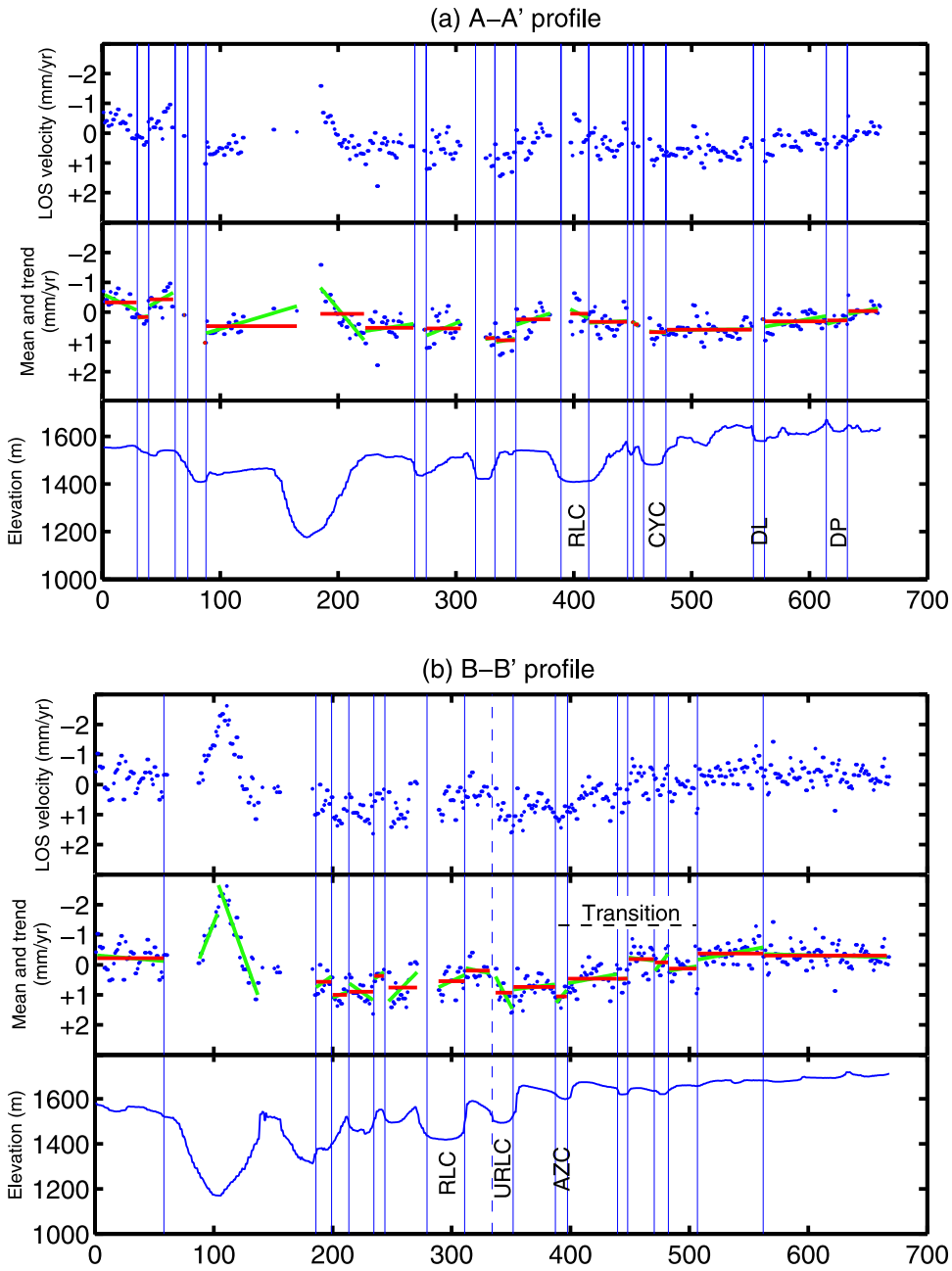

Figure 12. (Top) cross sections of LOS velocity fields, (middle) their mean (red) and trend (green) in each bin, and (bottom) elevations along selected surface tracks; surface tracks are shown in Figure 11. (a) A-A′, (b) B-B′, (c) C-C′, (d) D-D′, (e) E-E′, (f) F-F′, (g) G-G′. Canyon names for annotated abbreviations are as follows. RLC: Red Lake Canyon, CYC: Cyclone Canyon, DL: Devil's Lake Canyon, DP: Devil's pocket Canyon, URLC: Upper Red Lake Canyon, AZC: Aztec Canyon.

[1982]. LOS velocity and elevation values along each profile are shown in the top and bottom of Figure 12. The vertical lines in Figure 12 represent the intersection of each profile with the fault traces. Shown in the middle of Figures 12 are our computed mean and trend of the LOS velocities in each bin. The cross sections presented in Figures 12 support a number of observations, interpretations, and models of modern deformation in Canyonlands, while they refute others and provide additional details of the active tectonics in the Needles District.

5.1. Extensional Fault Array

[30] The region of higher subsidence is clearly located between the east side of the Colorado River Canyon to the west and the crest of the Monument Uplift to the east (Figures 3 and 4). *McCleary and Romie* [1986] used seismic reflection data to map the upper boundary of the Paradox Formation and discovered that the boundary dips in both the east and west directions, from the north-south trending crest of the Monument Uplift. *Schultz-Ela and Walsh* [2002, Figure 5] noted that the eastern limit of the grabens is

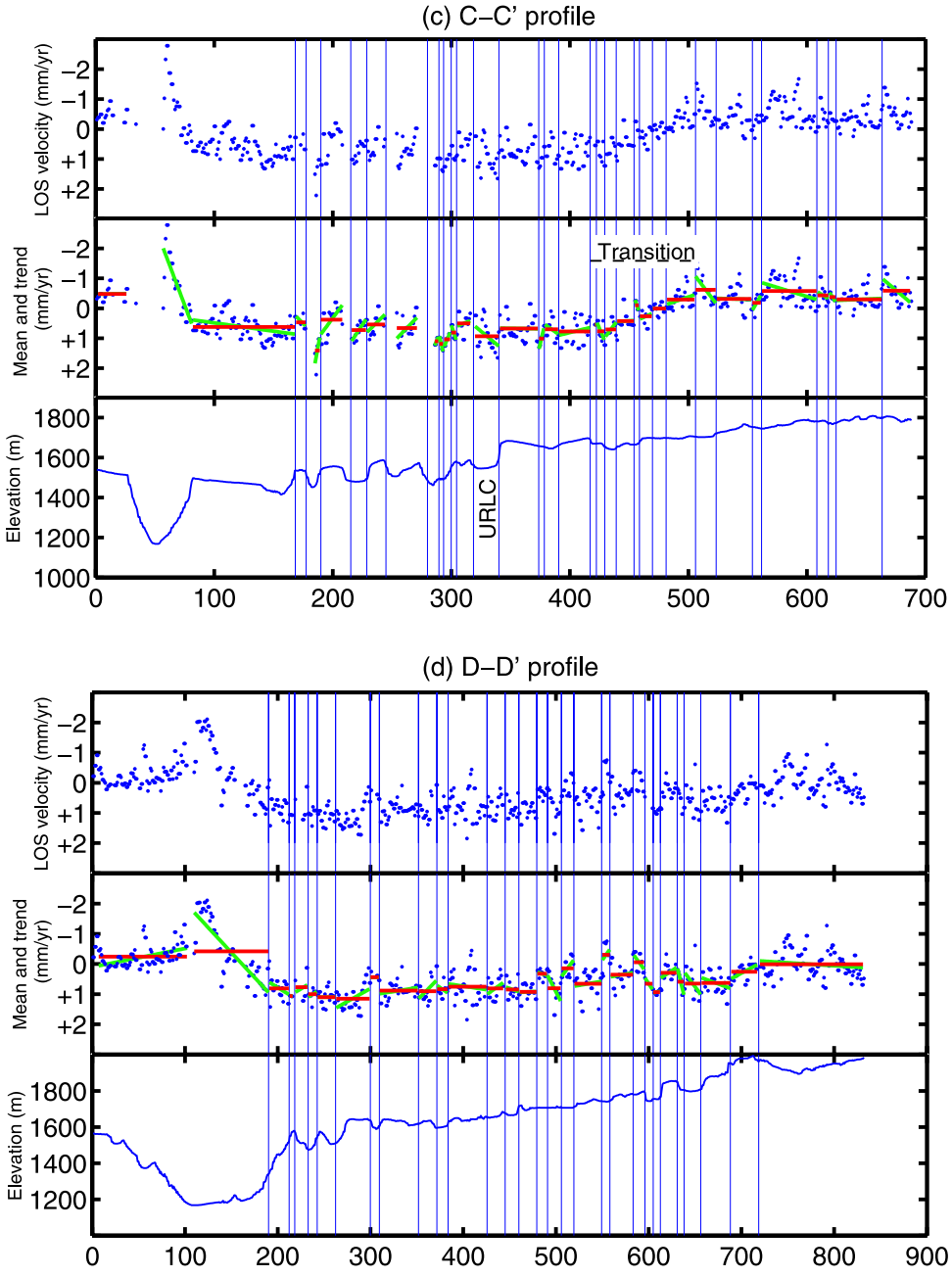

Figure 12. (continued)

coincident with the crest of this fold. The deformation pattern shown in Figures 3 and 4 thus supports the hypothesis that the presence of the free boundary along the river allows gravitationally induced, westward extension and salt flow west of the crest of the Monument Uplift, but that the absence of a free boundary east of the fold axis prevents similar deformation on the eastern side. In addition, uplift along the riverbank, associated salt withdrawal beneath the fault array, and dissolution along the river, could all play a significant role in the formation of the extensional faults. We can observe more details from a scrutiny of the cross sections shown in Figure 12.

[31] The deformation rates do not decrease uniformly with distance east of the river, but do decrease to near-zero on the eastern part of the study area, ~5 km from the river. The eastern boundary of the deforming zone is thus roughly coincident with the eastern limit of the grabens. While cross sections AA′, BB′, CC′, and DD′ show that some well-developed grabens are subsiding more rapidly than adjacent horsts, some other grabens to the east are not measurably deforming at present (Figures 12a–12d). Moreover, cross sections BB′ and CC′ suggest that a transition zone or gradient in the LOS changes bounding the extensional fault array exists between a deforming to nondeforming area to the southeast (Figures 12b and 12c). In the southwestern corner of the Needles District, however, such a transition zone does not exist and a broad gradient in the LOS changes is apparent from west to east away from the Colorado River.

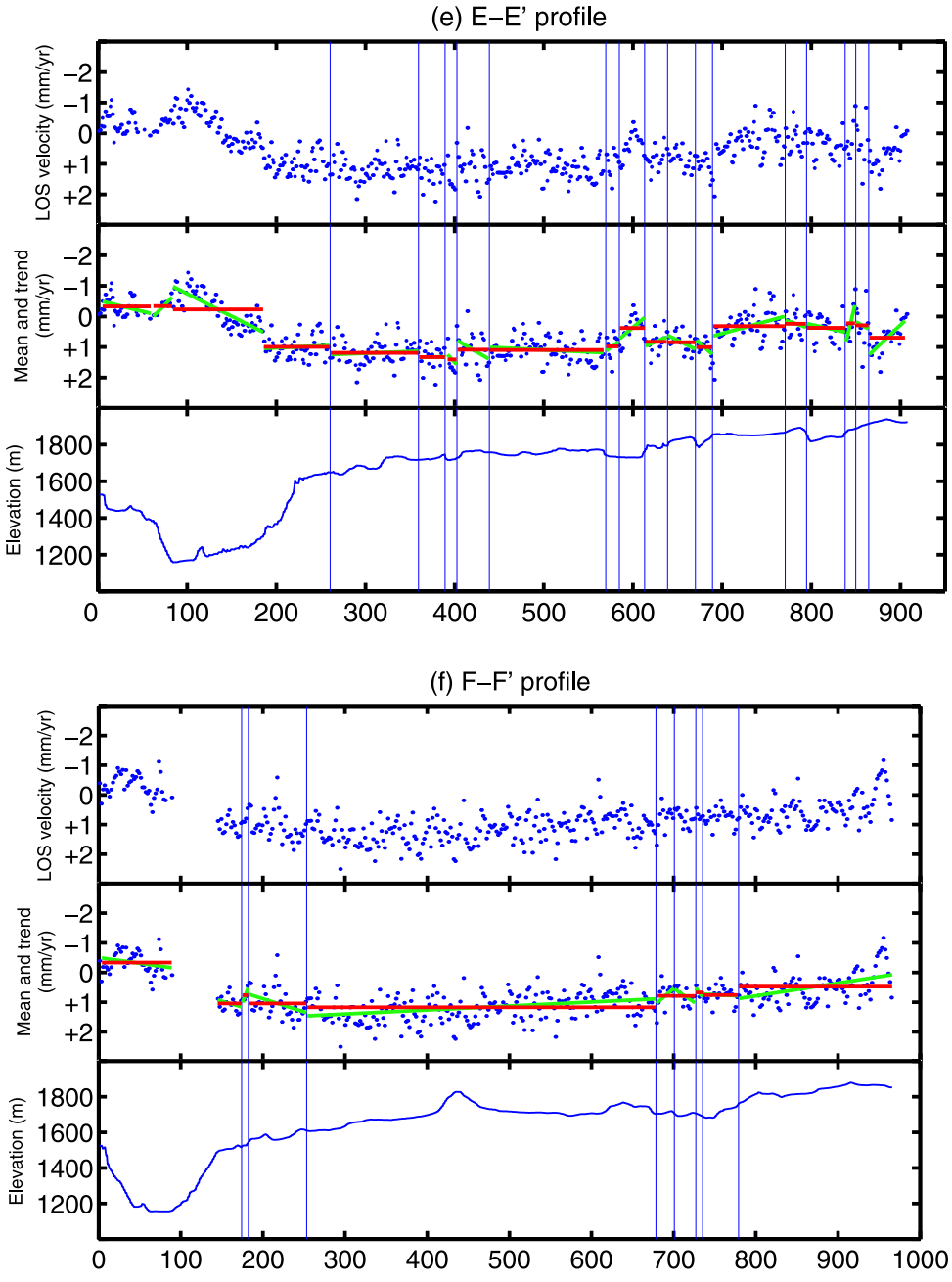

Figure 12. (continued)

Extending the inference by *Schultz-Ela and Walsh* [2002], this could reflect a change in the upper boundary of the Paradox Formation, or deformation that sweeps eastward as an abrupt dislocation front.

[32] Numerical modeling results have argued that grabens should be subsiding more rapidly than horsts [*Schultz-Ela and Walsh* 2002; *Walsh and Schultz-Ela* 2003]. Cross sections AA′, BB′, CC′, and DD′ suggest that this hypothesis does not always hold true. Profile AA′ shows that a deep graben, Red Lake Canyon, is not substantially deforming at present (Figure 12a). Profiles, BB′, CC′, and DD′ also do not suggest that grabens along these sections are subsiding more rapidly than horsts (Figures 12b, 12c, and 12d). In general, we do not see good correlation between higher subsidence in the floors of grabens. Cross sections BB′ and CC′ indicate that the eastern edge of Upper Red Lake Canyon (Figure 11b) is deforming faster than its middle portion (Figures 12b and 12c). This can be interpreted as suggesting that this graben may be subsiding at lower rates at its endpoints. As seen in Figures 12, Red Lake Canyon (Figure 11b) is a deep graben, and thus displacements on extensional faults bounding it might be expected to be greater than those for other grabens. The middle section of this graben does not appear to be undergoing significant deformation, whereas the eastern margin of Upper Red Lake Canyon is subsiding (rotating) at a rate of 2.0–2.5 mm/year. Although this is a localized pattern, this observation is consistent with an inference for graben evolution proposed

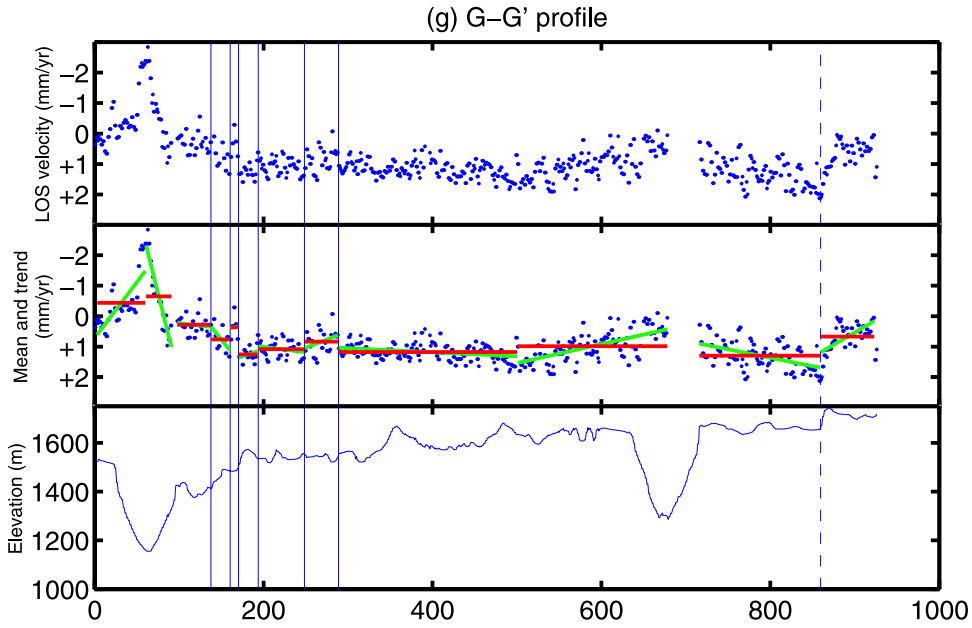

Figure 12. (continued)

by *Moore and Schultz* [1999, Figure 13]. The faults bounding a graben are predicted to nucleate at Earth's surface and to propagate downward to the salt layer in response to flexure of the overlying plate. This is accompanied by rotation of the extensional fault blocks as they subside into the underlying salt, first by westward tilting above east-dipping faults, then by eastward tilting above west-dipping faults that develop later in the stretching process above reactive diapirs in the salt itself [*Moore and Schultz*, 1999].

[33] In general, extensional faulting in the region is predicted to migrate eastward away from the river, with the most active modern deformation located further east. This should be evident as higher LOS change rates in the eastern part of the normal fault array. However, the InSAR results show that grabens further west are generally moving faster, whereas grabens to the east such as Devils Lane and Devils Pocket do not appear to be deforming measurably at present (Figure 12a). This could imply that differential deformation generally occurs along the abrupt gradient in the LOS changes that lie near the eastern side of the extensional fault array, rather than between individual grabens and horsts, though Red Lake Canyon (discussed above) is an apparent exception to this rule.

[34] We also notice a narrow zone of significant LOS shortening that follows the riverbank within the Colorado River Canyon (Figures 12a–12d). This presumably represents upward motion of the ground surface, and strongly suggests the presence of active salt diapirism and associated uplift of the surface [e.g., *Jackson et al.*, 1994]. We are unable to map radar LOS changes uniformly along both sides of the riverbank due to the radar layover and shadow effects inherent to steep east-facing slopes. However, Figures 12b and 12d clearly indicate that the region of LOS shortening resides on both sides of the riverbank. Although the floor of the river canyon consists largely of landslide deposits, there are numerous exposures of gypsum caprock of the Paradox Formation along the riverbank and tributaries [*Huntoon et al.*, 1982], suggesting the presence of underlying salt close to the surface. Observations of LOS shortening and its clear anticorrelation with the elevation profile along the eastern wall of the river canyon suggest that the thinner the sedimentary plate, the faster the uplifting velocity.

[35] As evident from the cross sections in Figures 12a–12d, the gradient in range change rate along the riverbank is apparently a couple of times higher than in the broad areas of subsidence elsewhere in the Needles. Since evaporites near the river are almost in direct contact with ground water, they can be significantly weakened by the presence of water, making their viscosity dramatically lower than that of natural dry salt [*Wenkert*, 1979; *Talbot and Rogers*, 1980; *Urai et al.*, 1986]. It is thus likely that at the bottom of the Colorado River the deformation rate is much higher than that observed along the riverbank. In the numerical modeling studies by *Schultz-Ela and Walsh* [2002], the viscosity of rock salt is assumed to be uniformly 10^{18} Pas in order to avoid numerical instability in the solution. It might therefore be important in future studies to explicitly take into account the spatial variations in the viscosity of underlying evaporites.

5.2. Area Southwest of the Grabens

[36] It is clear from Figures 3, 4, and 11a that despite the absence of the well-developed graben/horst system that exists northeast of this region, this area is undergoing significant widespread deformation at a maximum rate of 2.0–2.5 mm/year along the LOS.

[37] Figure 12e shows a profile running along a large side canyon in the southern part of the study area. Again, the lower topography correlates well here with the uplift signal, rising to a high of 1 mm/year at the crest next to the Colorado River. The absence of an uplift signal in Figure 12f is presumably due to the lack of radar data on the east side of the river. The profile in Figure 12f does not show any

significant trend in the velocity field, further arguing that the region is broadly flexing here. Figure 12g shows two uplifting regions, one along the Colorado River as in other profiles, and the other around a side canyon to the south. Although we do not see obvious haloes of subsidence as might be expected for more rapid localized salt withdrawal around side canyons, cross section GG' (Figure 12g) indicates that surface edges of the side canyon are locally uplifting with respect an otherwise large subsiding signal. The area nearby in the Colorado River canyon shows an even larger uplift signal (Figure 11a). As in section EE′, uplift around the Colorado River correlates with lower topography, suggesting that more uplift occurs where the overlying brittle plate is thinner.

[38] Figure 12g also clearly shows that this region is bounded to the south across an abrupt gradient in the LOS change that is coincident with the southern edge of an east-west trending graben located immediately east of the Colorado River canyon (dashed line in Figure 12g). This fault is apparently moving faster than any faults in the region at present (Figure 3). It should be noted that since we used interferogram pairs with short baselines it is unlikely that the deformation signal is an artifact due to errors in the DEM (Table 2). The east-west trending graben lies ~3 km north of the mapped location of a salt pinchout to the south (Figure 1) [*Condon*, 1997].

[39] Because of the higher average elevation of this area relative to the grabens region further northeast (Figure 1), the large displacement rates in this area could be interpreted as reflecting regional subsidence, prior to the initiation of surface extension and graben development. While numerical modeling studies predict an eastward (upslope) progression in the evolution of grabens [*Schultz-Ela and Walsh*, 2002; *Walsh and Schultz-Ela*, 2003], the present InSAR observations add data suggesting that grabens also develop in a southward direction in the southern part of the study area, consistent with the dip of the strata above the Paradox Formation (which here dips north).

[40] In another model consistent with initial breaching of the salt layer in the south, we speculate the pattern of deformation inferred from InSAR data may reflect two different modes of deformation due to salt withdrawal. The region to the south, which has nearly continuous exposure of Paradox Formation along the river (Figure 11b), is apparently deforming by broad subsidence of the sandstone plate without subsequent extension and block faulting. In contrast, the region to the north experiences less efficient removal of salt along the river, yet it undergoes dramatic stretching and normal faulting at the surface as well as overall subsidence. While we have not undertaken numerical modeling of the region, we speculate that the thickness of Paradox Formation (which pinches out to the south) may play a role in governing the boundary conditions that determine the two different styles in the region. In addition, rates of dissolution of salt along the length of the Colorado River in the Needles District undoubtedly affect local rates of plate subsidence and diapiric uplift along the walls of the canyon.

[41] Evidence of diapiric rise along the river is sparser to the southwest than to the northeast, which is due to the radar visibility of descending track data. This issue could be substantially resolved using ascending track data and so is deferred to a future study.

6. Concluding Remarks

[42] We applied standard InSAR and IPTA techniques to ERS1/2 SAR data from 1992 to 2002 to estimate displacement rates in the Needles District of Canyonlands National Park (Utah). The results of both techniques show that ongoing deformation is restricted to a region bounded by the Colorado River to the west and north, the crest of the Monument Uplift to the east, and the pinchout of evaporite facies to the south. Amplitudes over most of this region are on the order of 1~3 mm/year, away from the satellite. This corresponds to either ~1–3 mm/year of subsidence, or ~3–9 mm/year of westward motion, or a combination of both. Analyzing the power spectra of the "residual" signal and generating spatially correlated synthetic noise, we estimate the measurement precision as better than 0.8 mm/year but which could be worse along the riverbank.

[43] In the grabens area, the eastern boundary of the deformation zone coincides mostly with the eastern limit of the grabens, which, in turn, coincides with the crest of the Monument Uplift, a north-south trending fold. This is consistent with the hypothesis of salt flow driven by gravitational spreading and subsidence, initiated by the Colorado River cutting down through sediments to expose the salt layer. A long, thin ribbon of displacements toward the satellite at rates of 2–3 mm/year occurs along the edge of the Colorado River canyon. We interpret this as evidence of diapiric rise of salt as it is expelled from beneath the overriding sedimentary layer faster than it dissolves along the river.

[44] We find that the region southwest of the grabens area, where there is no well-developed system of grabens and horsts, generally shows the largest deformation rates. Because of the relatively higher overall elevation of this area, this could be interpreted as a precursor to graben formation. Alternatively, this region may deform in a fundamentally different fashion than the area to the north where extension at the surface is prevalent. The extreme southern edge of this region shows perhaps the largest displacement rates of all in an east-west trending graben. Previous numerical modeling studies have focused on the apparent eastward propagation of graben formation. Perhaps a future challenge for numerical models would be to simulate southward propagation as well or model the effects of salt thickness and pinchout to the south.

Appendix A: Processing Steps of Our IPTA Analysis

[45] In our IPTA analysis all 35 scenes are used in a single least squares fit, regardless of the spatial separation of the satellite's repeat orbit. The effects of DEM errors are minimized by solving for topographic corrections during the fitting process. Because the method compares phase information from many scenes at once, it requires ground scatterers that are persistent enough to be present in every scene. A region such as Canyonlands with abundant rock exposure is an ideal environment for this approach.

[46] Several variations of IPTA analyses are possible. Our approach is shown in the flow chart shown below; there are numerous IPTA processing strategies, and readers should keep in mind that ours is not the only possible approach. After gathering coregistered single look complex (SLC) data for the 35 available scenes of this region (step 1), we identify all candidate targets that could act as point targets (step 2); they are conceptually equivalent to permanent scatterers. By using data from only those candidate targets, the total SLC data set is significantly reduced to about 13% of the original number of pixels. We form differential interferograms, denoted as ϕ^j_{diff} with $j = 1,\ldots, 35$, by taking the difference between the j'th scene and the scene from 25 August 1995 (step 3). That reference scene is chosen because its satellite position was closest to the average satellite position of the other 34 scenes. The average perpendicular baseline length is 382.5 m.

[47] We use this set of differential interferograms to solve for a DEM height correction, dh, and a linear deformation rate, v, for each target (step 4). We assume:

$$\phi^j_{diff} = Atmos_0 + \frac{4\pi}{\lambda}\frac{B^j_p dh}{R\sin\alpha} + \frac{4\pi}{\lambda}\delta t^j v + residual_j, \quad (j = 1...N), \tag{A1}$$

where λ, B^j_p, R, α, and $\delta\, t^j$ are all known parameters: the radar wavelength, perpendicular baseline length, range from the satellite to the target, incidence angle, and time separation from 25 August 1995. Here, the spatially constant term $Atmos_0$ is for the atmospheric phase on 25 August 1995 and is also estimated as an offset plane of the regression analysis. The $residual_j$ represents the deviation from the height correction plus a linear velocity model and so includes atmospheric effects at each temporal epoch, orbit error slope, and nonlinear ground motion. We implement an iterative regression analysis to estimate both dh and v. After each iteration, we delete targets where the RMS of $residual_j$ lies above some minimum threshold, which can be defined differently for different iterations. Thresholds are needed both to obtain good results for the fitted parameters and for uniqueness when unwrapping phases (i.e., when determining how many integral values of 2π, if any, should be added to the phase). One consequence is that targets are likely to be rejected if they have large, nonlinear phase variability. At the end of our final iteration process, for example, we find that the imposition of these thresholds has reduced the total number of targets by a factor of about 50.

[48] Our iteration proceeds as follows (step 5–9). Since the differential phases are wrapped in the beginning stages of regression, we first subdivide the entire scene into a number of small patches, each with an area of ~75 pixels by 75 pixels (a pixel size is 4 m × 8 m). In this early stage in the analysis we include two minimum thresholds: one for the RMS of an individual target's residual$_j$ relative to the reference of the patch it lies within, and the other for the RMS of residual$_j$ between each patch's local reference points. Candidate targets and local references that exceed these thresholds are rejected. This removes targets with large variability relative to nearby targets early in the analysis. However, if all targets within a several hundred meter region behave the same way, they are retained for further analysis.

[49] After two iterations, the differential interferograms become relatively smooth because of the refined DEM and velocity models, and their phases can be readily unwrapped (step 10). After this we estimate "atmospheric phases," by spatially smoothing the values of residual$_j$ obtained from the third regression (step 11), over scales of several hundred meters. Although we refer to these smoothed fields as "atmospheric phases," they include any large-scale nonlinear variability, whether caused by the atmosphere or nonlinear ground displacements. These atmospheric phases are then subtracted from each differential interferogram, and the corrected ϕ^j_{diff} is used in (A1) to obtain improved values of dh and v (step 13). At this stage a global threshold is employed to omit points by finding the RMS of an individual target's residual$_j$ relative to the reference target. This provides the final, best estimate of the displacement rate for each target, along with a 35-point time series of displacement residuals relative to that rate.

[50] Below are the summaries of processing steps of the iteration procedures in our IPTA processing.

[51] 1. Gathering co-registered SLC data.

[52] 2. Selection of point candidates.

[53] 3. Generating initial (point) differential interferogram ϕ_{diff0} based on initial DEM$_0$.

[54] 4. First regression analysis in (B_p, t) space (patch-wise). Initial height correction estimates dh_0 and initial velocity estimate v_0 are derived, and first updated DEM$_1$ = DEM$_0$ + dh_0 is derived.

[55] 5. Generating refined ϕ_{diff1} based on DEM$_1$ and v_0.

[56] 6. Reestimate baseline $\tilde{B}_p$ from long-wavelength phase slope.

[57] 7. Generating refined ϕ_{diff2} based on DEM$_1$ and v_0.

[58] 8. Second regression analysis in ($\tilde{B}_p$, t) space (patch-wise). Second height correction estimates dh_1 and first velocity correction estimate dv_1 are derived, and DEM and velocity estimate are updated to be DEM$_2$(= DEM$_1$ + dh_1) and v_2(= v_0 + dv_1).

[59] 9. Generating refined ϕ_{diff3} based on DEM$_2$ and v_2.

[60] 10. Smoothing ϕ_{diff3} to generate unwrapped differential interferogram $\phi_{diff3unw}$.

[61] 11. Third regression analysis in ($\tilde{B}_p$, t) space (global processing). Third height correction estimates dh_2 and renewed velocity correction estimate dv_2 are derived, and DEM and velocity estimate are updated to be DEM$_3$(= DEM$_2$ + dh_2) and v_3(= v_2 + dv_2). Residual phases are spatially smoothed, from which "atmospheric" phases ϕ_{atm} are estimated.

[62] 12. Generating refined $\phi_{diff4unw}$ based on DEM$_3$, v_3 and ϕ_{atm}.

[63] 13. Final regression analysis in ($\tilde{B}_p$, t) space (global processing). Fourth height correction estimates dh_3 and renewed velocity correction estimate dv_3 are derived, and DEM and velocity estimate are further updated to be DEM$_4$(= DEM$_3$ + dh_3) and v_4(= v_3 + dv_3). Residual phases are spatially smoothed and passed through a temporal filter to estimate nonlinear deformation.

[64] 14. Final deformation product is v_4 + nonlinear deformation.

[65] **Acknowledgments.** Original SAR data are copyrighted by the European Space Agency, and acquired via the WInSAR Consortium with funding from NSF, NASA, and USGS. Partial support to M. Furuya was provided by a CIRES Visiting Fellowship and MEXT Japan. We thank M. Hudec and V. Gupta for helpful discussions on Canyonlands and salt tectonics. Comments from H. A. Koyi, R. Bürgmann, and an anonymous reviewer significantly improved our original manuscript.

References

Baars, D. L. (2003), Geology of Canyonlands National Park, Utah, in *Geology of Utah's Parks and Monuments*, 2nd ed., *Utah Geol. Assoc. Publ.*, vol. 28, edited by D. A. Sprinkel, T. C. Chidsey Jr., and P. B. Anderson, pp. 61–83, Utah Geol. Assoc., Salt Lake City, Utah.

Bürgmann, R., P. A. Rosen, and E. J. Fielding (2000), Synthetic Aperture radar interferometry to measure Earth's surface topography and its deformation, *Annu. Rev. Earth Planet. Sci.*, *28*, 169–209.

Cartwright, J. A., B. D. Trudgill, and C. S. Mansfield (1995), Fault growth by segment linkage: An explanation for scatter in maximum displacement and trace length data from the Canyonlands Grabens of SE Utah, *J. Struct. Geol.*, *19*, 1319–1326.

Colesanti, C., A. Ferretti, F. Novali, C. Prati, and F. Rocca (2003), SAR monitoring of progressive and seasonal ground deformation using the permanent scatterers technique, *IEEE Trans. Geosci. Remote Sens.*, *41*(7), 1685–1701, doi:10.1109/TGRS.2003.813278.

Commins, D., S. Gupta, and J. Cartwright (2005), Deformed streams reveal growth and linkage of a normal fault array in the Canyonlands graben, Utah, *Geology*, *33*(8), 645,doi:10.1130/G21433.1.

Condon, S. M. (1997), Geology of the Pennsylvanian and Permian Cutler Group and Permian Kaibab Limestone in the Paradox Basin, southeastern Utah and southwestern Colorado, *U.S. Geol. Survey Bull.*, *2000-P*, 46.

Crider, J. G., and D. D. Pollard (1998), Fault linkage: Three-dimensional mechanical interaction between echelon normal faults, *J. Geophys. Res.*, *103*(B10), 24,373–24,391.

Emardson, T. T., M. Simons, and F. H. Webb (2003), Neutral atmospheric delay in interferometric synthetic aperture radar applications: Statistical description and mitigation, *J. Geophys. Res.*, *108*(B5), 2231, doi:10.1029/2002JB001781.

Ferretti, A., C. Prati, and F. Rocca (2000), Nonlinear subsidence rate estimation using permanent scatterers in differential SAR interferometry, *IEEE Trans. Geosci. Remote Sens.*, *39*(5), 2202–2212.

Ferretti, A., C. Prati, and F. Rocca (2001), Permanent scatterers in SAR interferometry, *IEEE Trans. Geosci. Remote Sens.*, *39*(1), 8–20.

Hanssen, R. F. (2001), *Radar Interferometry—Data Interpretation and Error Analysis*, 308 pp., Kluwer, Dordrecht, Netherlands.

Hilley, G. E., R. Bürgmann, A. Ferretti, F. Novali, and F. Rocca (2004), Dynamics of slow-moving landslides from permanent scatterer analysis, *Science*, *304*, 1952–1955.

Hooper, A., H. Zebker, P. Segall, and B. Kampes (2004), A new method for measuring deformation on volcanos and other natural terrains using InSAR persistent scatterers, *Geophys. Res. Lett.*, *31*, L23611, doi:10.1029/2004GL021737.

Huntoon, P. W. (1982), The Meander anticline, Canyonlands, Utah: An unloading structure resulting from horizontal gliding on salt, *Geol. Soc. Am. Bull.*, *93*(10), 941–950.

Huntoon, P. W., G. H. Billingsley, and W. J. Breed (1982), Geologic map of Canyonlands National Park and vicinity, Canyonlands Natural History Assoc., Moab, Utah.

Jackson, M. P. A., B. C. Vendeville, and D. D. Schultz-Ela (1994), Structural dynamics of salt systems, *Annu. Rev. Earth Planet. Sci.*, *22*, 91–117.

Lohman, R. B., and M. Simons (2005), Some thoughts on the use of InSAR data to constrain models of surface deformation: Noise structure and data downsampling, *Geochem. Geophys. Geosyst.*, *6*, Q01007, doi:10.1029/2004GC000841.

Marsic, S. D. (2003), Active Deformation at Canyonlands National Park: Distribution of Displacements Across the Grabens Using Spaceborne Geodesy, Masters thesis, 166 pp., Univ. of Southern Calif., Los Angeles, Calif.

Marsic, S. D., S. E. Owen, and J. G. Crider (2003), Distribution of displacement across Canyonlands Grabens using GPS and InSAR, *Eos Trans. AGU*, *84*(46), Fall Meet. Suppl., Abstract G21D–289.

Massonnet, D., and K. L. Feigl (1998), Radar interferometry and its application to changes in the earth's surface, *Rev. Geophys.*, *36*, 441–500.

McCleary, J. R., and J. E. Romie (1986), Stratigraphic and structural configuration of the Navajo (Jurassic) through Ouray (Mississippian-Devonian) Formations in the vicinity of Davis and Lavender Canyons, southeastern Utah, Battelle Memorial Institute, *Tech. Rep. ONWI-594*, Off. of Nucl. Waste Isolation, Columbus, Ohio.

McGill, G. E., and A. W. Stromquist (1979), The grabens of Canyonlands National Park, Utah: Geometry, mechanics, and kinematics, *J. Geophys. Res.*, *84*(B9), 4547–4563.

Moore, J. M., and R. A. Schultz (1999), Processes of faulting in jointed rocks of Canyonlands National Park, Utah, *Geol. Soc. Am. Bull.*, *111*(6), 808–822.

Musson, R. M. W., M. Haynes, and A. Ferretti (2004), Space-based Tectonic Modeling in Subduction Areas Using PSInSAR, *Seismol. Res. Lett.*, *75*(5), 598–606.

Scharroo, R., and P. Visser (1998), Precise orbit determination and gravity field improvement for the ERS satellites, *J. Geophys. Res.*, *103*, 8113–8127.

Schultz, R. A., and J. M. Moore (1996), New observations of grabens from the Needles District, Canyonlands, National Park, Utah, in *Geology and Resources of the Paradox Basin, Utah Geol. Assoc. Guidebook*, vol. 25, edited by A. C. Huffman, W. R. Lund, and L. H. Godwin, pp. 295–302, Utah Geol. Assoc., Salt Lake City, Utah.

Schultz-Ela, D. D., and P. Walsh (2002), Modeling of grabens extending above evaporites in Canyonlands National Park, Utah, *J. Struct. Geol.*, *24*, 247–275.

Talbot, C. J., and E. A. Rogers (1980), Seasonal movements in a salt glacier in Iran, *Science*, *208*, 395–397.

Trudgill, B., and J. Cartwright (1994), Relay-ramp forms and normal-fault linkages, Canyonlands National Park, Utah, *Geol. Soc. Am. Bull.*, *106*(9), 1143–1157.

Trudgill, B. D. (2002), Structural controls on drainage development in the Canyonlands grabens of southeast Utah, *Am. Assoc. Petrol. Geol. Bull.*, *86*(6), 1095–1112.

Urai, J. L., C. J. Spiers, H. J. Zwart, and G. S. Lister (1986), Weakening of rock salt by water during long-term creep, *Nature*, *324*, 554–557.

Walsh, P., and D. D. Schultz-Ela (2003), Mechanics of graben evolution in Canyonlands National Park, Utah, *Geol. Soc. Am. Bull.*, *115*(3), 259–270.

Wegmüller, U., and C. L. Werner (1997), Gamma SAR processor and interferometry software, in *Proceedings of the 3rd ERS Symposium*, *Eur. Space Agency Spec. Publ., ESA SP-414*, 1686–1692.

Wenkert, D. D. (1979), The flow of salt glaciers, *Geophys. Res. Lett.*, *6*(6), 523–526.

Werner, C. L., U. Wegmüller, T. Strozzi, and A. Wiesmann (2003), Interferometric point target analysis for deformation mapping, paper presented at IGARSS'03, Geosci. and Remote Sens. Soc., Toulouse, France.

M. Furuya, Earthquake Research Institute, University of Tokyo, Yayoi 1-1-1, Bunkyo-ku, Tokyo 113-0032, Japan. (furuya@eri.u-tokyo.ac.jp)

K. Mueller, Department of Geological Sciences, University of Colorado, Boulder, CO 80309-399, USA. (karl.mueller@colorado.edu)

J. Wahr, CIRES and Department of Physics, University of Colorado, Boulder, CO 80309-390, USA. (wahr@longo.colorado.edu)